

Comprehensive analysis of field-electron emission properties of nanosized silicon blade-type and needle-type field emitters

Gleb D. Demin, Nikolay A. Djuzhev, Nikolay A. Filippov, Petr Yu. Glagolev, Iliya D. Evsikov, and Nikolay N. Patyukov

Citation: *Journal of Vacuum Science & Technology B* **37**, 022903 (2019); doi: 10.1116/1.5068688

View online: <https://doi.org/10.1116/1.5068688>

View Table of Contents: <https://avs.scitation.org/toc/jvb/37/2>

Published by the [American Vacuum Society](#)

HIDEN
ANALYTICAL

Instruments for Advanced Science

Contact Hiden Analytical for further details:

W www.HidenAnalytical.com

E info@hiden.co.uk

CLICK TO VIEW our product catalogue



Gas Analysis

- ▶ dynamic measurement of reaction gas streams
- ▶ catalysis and thermal analysis
- ▶ molecular beam studies
- ▶ dissolved species probes
- ▶ fermentation, environmental and ecological studies



Surface Science

- ▶ UHV TPD
- ▶ SIMS
- ▶ end point detection in ion beam etch
- ▶ elemental imaging - surface mapping



Plasma Diagnostics

- ▶ plasma source characterization
- ▶ etch and deposition process reaction kinetic studies
- ▶ analysis of neutral and radical species



Vacuum Analysis

- ▶ partial pressure measurement and control of process gases
- ▶ reactive sputter process control
- ▶ vacuum diagnostics
- ▶ vacuum coating process monitoring

Comprehensive analysis of field-electron emission properties of nanosized silicon blade-type and needle-type field emitters

Gleb D. Demin,^{a)} Nikolay A. Djuzhev,^{b)} Nikolay A. Filippov, Petr Yu. Glagolev, Iliya D. Evsikov, and Nikolay N. Patyukov
MEMSEC R&D Center, National Research University of Electronic Technology (MIET), Shokina Sq., 6, Zelenograd, Moscow 124527, Russia

(Received 17 October 2018; accepted 14 January 2019; published 11 February 2019)

The reproducibility of complementary metal-oxide-semiconductor (CMOS) technology makes it very promising for creating commercially available vacuum emission micro/nanoelectronic devices. However, there are a number of challenges that occur with CMOS, including current hysteresis, transition to the generation of self-sustained plasma, and thermal melting of the cathode. These issues affect the process of field-electron emission and lead to instability and subsequent degradation of field-emission cathodes. More detailed study is needed in order to address these negative effects. In this study, an array of nanoscale silicon needle-type cathodes and a single blade-type cathode were placed in vacuum to characterize their field-emission properties. The hysteresis nature of the field-emission current and the smooth transition from field emission to the generation of self-sustained plasma in the interelectrode space were simultaneously observed. Based on these experimental results, the authors propose the possible origins and mechanisms underlying these two phenomena. It was theoretically found that at field-emission currents corresponding to the observed melting point of the silicon nanocathodes, the melting point of silicon is not reached, which indicates the need to take into account additional effects of field emission, such as sputtering of the anode material. The results are useful for developing field-emission nanodevices based on silicon CMOS technology. *Published by the AVS.* <https://doi.org/10.1116/1.5068688>

I. INTRODUCTION

Recently, there has been renewed interest in vacuum nanoelectronics, particularly with regard to the development of field-emission nanodevices. This is due to the progress achieved in the nanofabrication technology used to create nanoscale vacuum diode and triode structures.^{1–6} The use of nanoscale vacuum channel makes it possible for vacuum nanoelectronic devices to approach their semiconductor counterparts in terms of power consumption and performance. This channel also eliminates the need for vacuum packaging, since the probability of electrons colliding with gas molecules at such small scales is practically negligible.⁷ The main advantages of field-emission nanodevices over solid-state electronics are attributed to their ability to operate at extremely high frequencies (in the THz range). This is made possible by the high charge mobility in vacuum. Vacuum nanoelectronics is also suitable for applications in harsh environments including high temperature and radiation, which pose challenges for modern solid-state devices and limit their performance.^{8,9}

Despite significant progress and prospects for the use of such vacuum nanoelectronic devices (based on the field-emission effect), there are still a number of obstacles to overcome before they can be put into commercial use. For example, the proposed manufacturing methods, materials,

and designs of vacuum field-emission cathodes do not allow for sufficient stability of current emission and durability of devices that use them. The undesirable effects of the field-emission process need to be studied further to understand how they impact the field-emission characteristics of nanoscale emitters.

The existence of a smooth transition from field emission to the plasma generation mode has been demonstrated at atmospheric pressure in the case of metal field emitters.^{10,11} More interestingly, a similar transition to stable plasma discharge was detected under low vacuum conditions during field emission from silicon pencil-shaped cathodes in the case of high emission currents.¹² As another physical effect, the hysteresis behavior of the field-emission characteristics of carbon nanostructures has been illustrated in a number of experimental works.^{13,14} This behavior can be explained by the processes of gas adsorption–desorption on the surface of emitters. However, the simultaneous presence of these phenomena for individual types and materials of nanoscale field emitters under low vacuum conditions had not previously been considered in detail.

Another important issue is the need to develop new theoretical approaches to field emission for nanoscale emitters. The existing classical Fowler–Nordheim emission theory is not compatible with an experiment on these scales (less than 20 nm) where dimensional and quantum-mechanical effects due to the transition to atomic sizes of the emission area must be taken into account.¹⁵ The causes of cathode melting during field emission also are not fully understood. These phenomena may be due to the combined effect of thermal

Note: This paper is part of the Special Topic Collection: Papers from the 31st International Vacuum Nanoelectronics Conference 2018.

^{a)}Electronic mail: gddemin@edu.miet.ru

^{b)}Electronic mail: djuzhev@ntc-nmst.ru

heating of the cathode by hot electrons in the near-surface layer of the emitter and the bombardment of its surface by high-energy ionized anode particles that occur when the anode material is sputtered during the field emission.

Currently, most studies of the field-emission process focus on metal and carbonlike nanoscale emitters that demonstrate longer lifetime and high field-emission efficiency.¹⁶ Nevertheless, it should be noted that mass production of vacuum field-emission nanodevices is possible only with the use of silicon complementary metal-oxide-semiconductor technology, which, due to its high reproducibility and wide distribution in modern electronics, remains the only technology suitable for these purposes.¹⁷ Thus, considering the phenomena accompanying the field-emission process as applied to nanosized silicon cathodes in various configurations is of particular practical interest.

Section I describes the technology route for creating the array of nanoscale silicon needle-type field emitters and a single sample of the silicon blade-type field emitter. The experimental set-up for measuring the field-emission characteristics of these structures is described. The theoretical model of the semiconductor cathode heating induced by the field-emission current is also presented. In Sec. II, we discuss the results of experimental studies of current-voltage characteristics of the silicon field nanoemitters, which are used to analyze the possible causes for the transition from field emission to the generation of self-sustained plasma and the corresponding appearance of hysteresis current loops during the experiment for several measurement cycles. The theoretical aspects of the thermal heating of silicon nanocathodes in the process of field emission are also briefly described. Finally, Sec. III provides the conclusions on this work and possible proposals for further research.

II. MATERIALS AND METHODS

A. Sample preparation

Arrays of nanoscale needle-type field emitters were fabricated using the following steps: phosphorus-doped (n-type) silicon wafers with (100) orientation and 150 mm diameter were oxidized in oxygen with water vapor (thickness of obtained SiO₂ layer was 0.3 μm). Then, a Si₃N₄ layer was deposited on them as a masking layer (thickness of 0.1 μm), after which photolithography was performed to form T-shaped oxide-nitride caps for silicon nanotips. The profile of the tip was formed using plasma-chemical etching in a mixture of SF₆ and O₂ with an anisotropy coefficient of 2.5.

The oxidation process for sharpening the silicon cathode was performed in dry oxygen ambient (silicon tips obtained after oxidation in wet oxygen had large dispersion of the tip curvature). Then, the SiO₂ layer (about 200 nm) was removed from the sample along with the mask layer.

In turn, blade-type cathodes were made using anisotropic etching of thinned silicon wafers with (100) orientation in 10% KOH at a temperature of 80 °C to the full depth along the (111) crystallographic planes.

The front and back sides of the thinned wafer were oxidized in dry oxygen, followed by photolithography on the front side to form V-shaped trenches. Due to the features of anisotropic etching, silicon blade-type field emitters were obtained with an apex angle of 54.74°. Figure 1 shows SEM images of the obtained structures: the array of nanoscale silicon needle-type emitters [see Fig. 1(a)] and a single silicon blade-type field emitter with the nanoscale tip curvature [see Fig. 1(b)].

B. Experimental set-up

The electrode system in the experimental set-up contains a test sample of field-emission nanoscale structures (the array of silicon needle-type field emitters or single blade-type cathode) set on the metal cylinder with filament. The cylinder was then put into a ceramic holder (cathode node from vacuum tube) to provide indirect heating, as shown for the blade-type emitter in Fig. 1(b). The distance between the cathode and anode was regulated by a mechanical micro screw. Depending on the type of sample under investigation, the anode was made either of 0.7 mm tungsten wire with a polished flat tip (in the case of the array of needle-type emitters) or a silicon wafer with a deposited platinum layer (in the case of a blade-type cathode). The electrode system was placed in a vacuum chamber with a pressure of 3·10⁻⁴ Pa. A 1-MΩ ballast resistor and 10-kΩ measuring resistor were connected to the electrode circuit. The voltage drop across the measuring resistor was measured using a ZET 017-U2 spectral analyzer. The measured voltage signal was then converted into a current of silicon field emitters (Fig. 2).

Measurement of the voltage drop on the electrodes is performed in the voltage divider circuit. After completing the current-voltage characterization experiment, the measured values of the signals were converted to the corresponding values of current and voltage.

C. Theory and computational methods

The thermal effects of the field-electron emission were confirmed by the results of our experimental studies. In the nanosized silicon tips, we observed thermal degradation of the cathode accompanied by melting of the cathode emission region and the appearance of microdroplets on its surface. The SEM images of the emitter in Fig. 3 clearly show the moments when the field-emission current was switched on and switched off.

To verify these results, we used COMSOL MULTIPHYSICS software¹⁸ to develop a self-consistent three-dimensional model that describes the field emission from silicon nanotips, taking into account the thermal phenomena associated with the penetration of an electric field into a semiconductor.

To calculate the electric potential $V_S(x, y, z) = -\varphi_S(x, y, z)/e$ that is responsible for the local band bending in the n-type (p-type) silicon field emitter due to the penetration of the electric field E_{vac} from vacuum into the near-surface layer of the semiconductor, the Poisson equation from Ref. 19 was implemented in our model in spherical

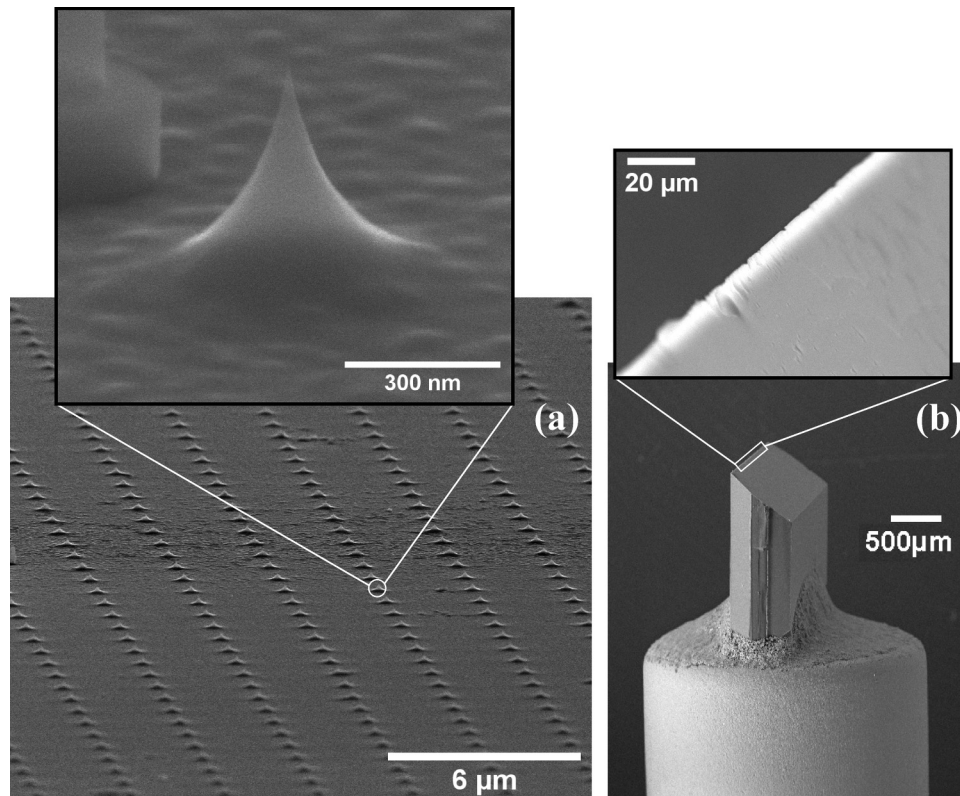


FIG. 1. SEM images of the obtained test samples for measuring the current–voltage characteristics: (a) the array of silicon needle-type field emitters and (b) a single silicon blade-type field emitter. The inset shows an enlarged scale of the marked areas.

coordinates

$$\frac{d^2\eta_\varphi}{dr_\delta^2} + \frac{2}{r_\delta} \frac{d\eta_\varphi}{dr_\delta} = f(\eta_\varphi, N_a, N_d). \quad (1)$$

From Eq. (1), φ_S is the potential energy of the electron;

$\eta_\varphi = \varphi_S/k_B T$; $r_\delta = r/\delta$; $r = \sqrt{x^2 + y^2 + z^2}$ is the point's distance from the origin inside the field emitter; $N_{d(a)}$ is the donor (acceptor) concentration; $\delta = (\zeta\epsilon_0 k_B T/2n_i e^2)^{1/2}$ is the Debye screening length of the semiconductor; ζ is the dielectric constant of the semiconductor; ϵ_0 is the vacuum permittivity; k_B is the Boltzmann constant; T is the temperature of

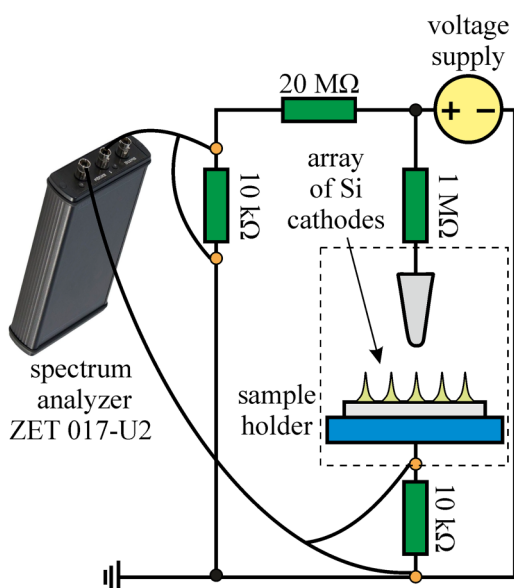


FIG. 2. Schematic presentation of the experimental set-up for the field-emission measurement of the array of silicon needle-type or blade-type field emitters.

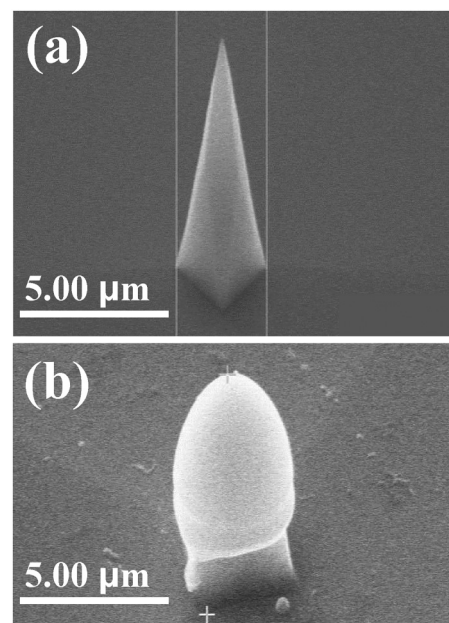


FIG. 3. SEM images of the silicon field emitter located on the cantilever (a) before and (b) after field-electron emission.

the emitter; e is the electron charge; and n_i is the intrinsic carrier concentration in the semiconductor at a given temperature. In the case of the fully ionized impurities, the function $f(\eta_\varphi, N_a, N_d)$ on the right side of Eq. (1) is determined by the simple expression

$$f(\eta_\varphi, N_a, N_d) = \frac{\Phi(\eta_\varphi^B, \eta_\varphi^F, \eta_e^F, \eta_e^V, \eta_e^C) - 2 \sinh(\eta_\varphi^B)}{2}, \quad (2)$$

where $\eta_e^F = \varepsilon_F/k_B T$, $\eta_e^{(v)} = \varepsilon_{c(v)}/k_B T$, $\eta_\varphi^B = \sinh^{-1}((N_a - N_d)/2n_i) = \varphi_B/k_B T$, $\varphi_B = \varepsilon_{Fi} - \varepsilon_F$, ε_{Fi} is the intrinsic Fermi level, ε_F is the Fermi level, $\varepsilon_{c(v)}$ is the bottom (top) of the (valence) conduction band, and $\Phi = \Phi(\eta_\varphi^B, \eta_\varphi^F, \eta_e^F, \eta_e^V, \eta_e^C)$ is the function determined through the half-order Fermi-Dirac integrals. To solve Eq. (1) numerically, we used the next boundary condition in the bulk $d\eta_\varphi/dr_\delta(r_\delta \rightarrow -\infty) = 0$.

In turn, the temperature of the silicon nanotip (mainly due to the Joule heating by the field-emission current) was calculated based on the self-consistent heat conduction equation

$$\rho C_p(T) \frac{\partial T}{\partial t} - \nabla \cdot (\kappa \nabla T) = \rho_\varphi(E_{vac}) J_e^2(E_{vac}), \quad (3)$$

where ρ is the volumetric mass density of the emitter material, $C_p(T)$ is the heat capacity of the emitter material at constant pressure, κ is the thermal conductivity of the emitter material, $\rho_\varphi = (e\mu_T n_\varphi)$ is the resistivity of the emitter material, $\mu_T = \mu_T(T, N_{a(d)})$ is the carrier mobility, $n_\varphi = N_{d(a)} \exp(-\eta_\varphi)$ is the equilibrium carrier concentration for an n-type (p-type) semiconductor,²⁰ where $\eta_\varphi = \eta_\varphi(E_{vac})$ should be obtained from Eq. (1), and $J_e = J_e(\eta_\varphi)$ is the field-emission current density, which was taken from the quantum-mechanical calculations of the field-electron emission from the silicon nanotip.²¹

III. RESULTS AND DISCUSSION

Based on the experimental set-up, the current–voltage characteristics were measured for samples of a single blade-type field emitter and the array of needle-type nanocathodes made using silicon technology (images shown in Fig. 1). Figure 4 shows the variation in emission current from a single silicon blade-type emitter with the anode voltage for three measurement cycles when the cathode–anode distance was $40 \mu\text{m}$. As illustrated in Fig. 4, there was a smooth transition from the field emission to the plasma discharge excitation in all three cases. Such a transition is characterized by a linear dependence of the emission current on the anode voltage, which follows the hysteresis region in the upper part of the graphs. Such an effect with nonhysteresis current behavior during the transition between the field-emission mode and the generation of a microarc discharge was previously described in Ref. 12 as a result of field-emission measurements for silicon pencil-shaped emitters under low vacuum conditions. In the current study, for all three curves, current–voltage hysteresis was observed, which may be due to the adsorption effects on the surface of the blade nanocathode, arising from some contamination from the field-emission process. At the same time, a slight expansion

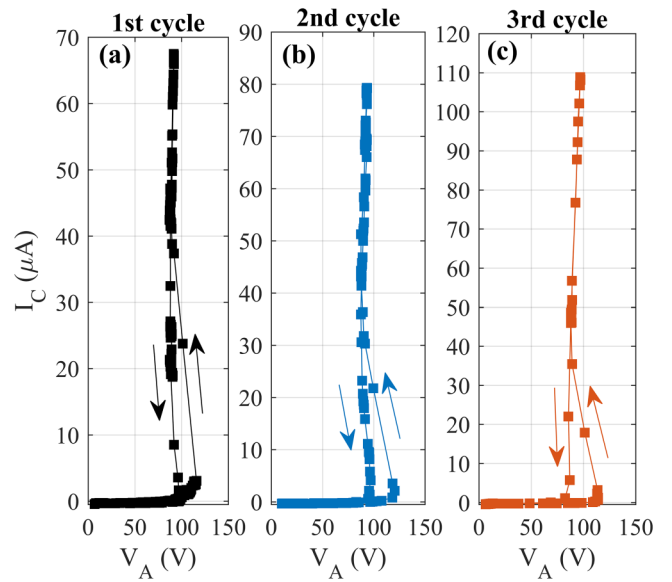


FIG. 4. Current–voltage characteristics of the silicon blade-type field emitter obtained for three measurement cycles [(a)–(c)] at a distance of $40 \mu\text{m}$ between the anode and cathode. The arrows show the direction of passage of the current loop during the measurements.

of the current loops occurred during the transition from the first to the third measurement cycle.

Similar measurements of the field-emission current were performed for the array of silicon needle-type emitters [see Fig. 5(a)], where the distance between the anode and cathode was $30 \mu\text{m}$. In this case, the current–voltage characteristics also exhibited hysteresis; however, no narrowing of the current loop was observed when approaching the

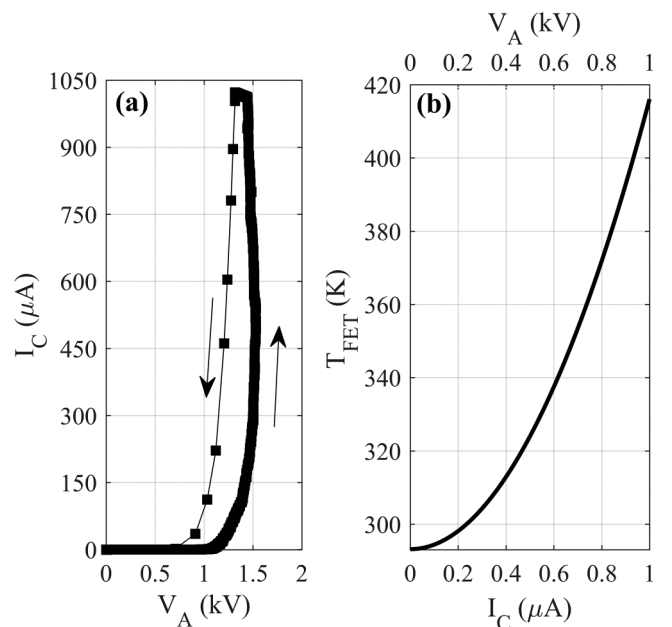


FIG. 5. (a) Current–voltage characteristics of the array of silicon needle-type field emitters obtained at a distance of $30 \mu\text{m}$ between the anode and cathode. The arrows show the direction of passage of the current loop during the measurements. (b) The maximum temperature of the silicon needle-type emitter vs the field-emission current I_D (anode voltage V_A).

plasma generation threshold. Thus, the change in the maximum temperature of the cathode tip [Fig. 5(b)], calculated within the framework of the developed theoretical model for the observed field-emission currents, does not exceed the melting point of Si. However, in certain cases, these currents can lead to serious deformation of the cathode, which is confirmed by the experiment and was previously illustrated in Fig. 3. Therefore, additional factors should be considered, such as sputtering of the anode material during the emission process.

Significant power densities up to 300 W/cm^2 were achieved at the anode surface, which was evaluated taking into account the variation in the spot size area at different emission currents. This feature can lead to heating of the anode surface by hot emitted electrons, which, in turn, accelerates the desorption processes on it. The bombardment of the anode by field-emission products from the cathode leads to the sputtering of its material and induce the flow of high-energy ionized anode particles toward the emitter surface as

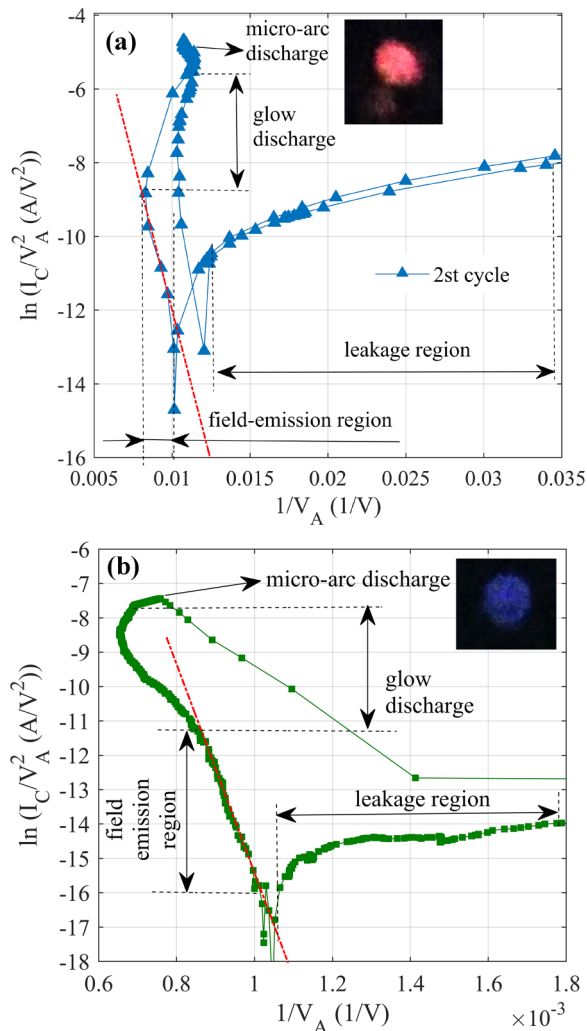


Fig. 6. Fowler–Nordheim plot of the current–voltage characteristics obtained for (a) the single silicon blade-type field emitter and (b) the array of silicon needle-type field emitters, respectively. The insets show photos of the plasma discharge in each case. The dotted line indicates the field-emission region.

an additional heat source. The threshold of emission current, providing the transition from field emission to self-sustained plasma generation in the microscale electrode gap,¹⁰ was also observed in our experiment, which may be caused by the anode sputtering. Figure 6 shows the current–voltage characteristics of silicon field nanoemitters from Figs. 4 and 5, recalculated in the Fowler–Nordheim coordinates. On these characteristics, four regions of the current versus voltage are easily distinguished: 1, leakage region; 2, field-emission region; 3, glow discharge area; and 4, micro-arc discharge area. As it can be seen from Fig. 6, a smooth transition to the emergence of self-sustained plasma for an array of needle-type emitters occurs at currents of the order of $1 \mu\text{A}$, while for single blade-type emitters, this transition occurs much later—at a current of about $3.5 \mu\text{A}$. A distinctive feature of the field emission from blade cathodes is that there is a linear increase in current toward high voltages when switching to an arc discharge area. This contrasts to the effects that occur during plasma generation in the case of measurements of an array of needle-type silicon nanocathodes. A variation in the discharge plasma color was also observed in the experiment for different cases (when measuring blade-type nanocathodes, arc discharge plasma is red in color, compared to blue for the needle-type nanocathodes). This may be explained by the different anode materials used in the two field-emission experiments conducted here. The increase in leakage current is associated with the specific features of the experimental set-up and the design of the cathode–anode electronic system.

These results should be taken into account when designing vacuum nanoelectronic devices, and these effects will be discussed in more detail in subsequent studies for various types of silicon emitters.

IV. CONCLUSIONS

A study of the current–voltage characteristics of silicon blade-type and needle-type field nanoemitters was conducted under low vacuum conditions. In the process of experimental studies, a smooth transition was observed from the field-emission mode to the plasma generation mode with a change in the type of discharge from glow to arc. The possible causes of the generation of self-sustained emission in the space between the anode and cathode were analyzed. Experimental results and theoretical calculations confirmed that sputtering of the anode in the process of field emission led to melting of the cathode. For given emission currents observed in the experiment with the array of silicon needle-type field emitters, it was theoretically shown that the calculated tip temperature of such emitters does not exceed the melting point of Si, which indicates the influence of additional heat sources. In the case of the single blade nanocathode, a distinctive feature of the transition to a microarc discharge was a linear increase in the current in the direction of voltage growth. This differs from the standard plasma generation process in the interelectrode space (as is described in several previous works^{10,12}). The current hysteresis observed during such a transition may be due to adsorption

processes occurring as a result of sputtering of the anode on the surface of the emission region.

The considered effects play an important role in the development of vacuum nanoelectronic devices operating on the principles of field emission. Further research is required to describe the features of field emission from nanoscale emitters and to develop new theoretical approaches to characterize the experimentally observed mechanisms of emission side effects (such as thermal instability, plasma generation, and current hysteresis).

ACKNOWLEDGMENTS

This work was performed based on the equipment of the R&D Center “MEMSEC” (MIET) and using the facilities of the R&D Center “Sensorics” (MIET), with the financial support of the Ministry of Education and Science of the Russian Federation (Grant No. 14.594.21.0012, id RFMEFI59417X0012).

- ¹J.-W. Han, J. S. Oh, and M. Meyyappan, *Appl. Phys. Lett.* **100**, 213505 (2012).
²J.-W. Han, D.-I. Moon, and M. Meyyappan, *Nano Lett.* **17**, 2146 (2017).
³W. M. Jones, D. Lukin, and A. Scherer, *Appl. Phys. Lett.* **110**, 263101 (2017).
⁴J. Lin, P. Y. Wong, P. Yang, Y. Y. Lau, and P. Zhang, *Proceedings of the 30th International Vacuum Nanoelectronics Conference*, Regensburg, Germany, 10–14 July 2017 (IEEE, Regensburg, 2017), p. 220.
⁵D. Patti, S. Pennisi, S. Lombardo, and G. Nicotra, *Proceedings of the 14th International Conference on Synthesis, Modeling, Analysis and Simulation Methods and Applications to Circuit Design*, Giardini Naxos, Taormina, Italy, 12–15 June 2017 (IEEE, Giardini Naxos, 2017), pp. 1–4.

- ⁶S. Srisonphan and K. Jitkajornwanich, *IEEE Trans. Electron Devices* **65**, 2601 (2018).
⁷L. Qian, Y. Wang, L. Liu, and S. Fan, *J. Vac. Sci. Technol. B* **28**, 562 (2010).
⁸A. Evtukh, H. Hartnagel, O. Yilmazoglu, H. Mimura, and D. Pavlidis, *Vacuum Nanoelectronic Devices: Novel Electron Sources and Applications* (Wiley, Chichester, 2015).
⁹J. Xua, Q. Wanga, Z. Qi, Y. Zhai, and X. Zhang, *J. Appl. Phys.* **117**, 204504 (2015).
¹⁰M. A. Bilici, J. R. Haase, C. R. Boyle, D. B. Go, and R. M. Sankaran, *J. Appl. Phys.* **119**, 223301 (2016).
¹¹A. M. Loveless and A. L. Garner, *IEEE Trans. Plasma Sci.* **45**, 574 (2017).
¹²W. Knapp, *Proceedings of the 30th International Vacuum Nanoelectronics Conference*, Regensburg, Germany, 10–14 July 2017 (IEEE, Regensburg, 2017), pp. 34–35.
¹³J. Li, X. Yan, G. Gou, Z. Wangb, and J. Chena, *Phys. Chem. Chem. Phys.* **16**, 1850 (2014).
¹⁴J. Chen, B. Yang, X. Liu, J. Yang, and X. Yan, *Appl. Phys. Lett.* **108**, 193112 (2016).
¹⁵B. Lepetit, *J. Appl. Phys.* **122**, 215105 (2017).
¹⁶S. G. Kim, S. A. Park, Y.-C. Kim, and B.-K. Ju, *J. Vac. Sci. Technol. B* **35**, 011802 (2017).
¹⁷R. Schreiner, C. Langer, C. Prommesberger, R. Ławrowski, F. Dams, M. Bachmann, F. Düsberg, M. Hofmann, A. Pahlke, P. Serbun, S. Mingels, and G. Müller, *Proceedings of the 28th International Vacuum Nanoelectronics Conference*, Guangzhou, China, 13–17 July 2015 (IEEE, Guangzhou, 2015), pp. 1–2.
¹⁸*COMSOL Multiphysics® v. 5.4* (COMSOL AB, Stockholm, 2018), see www.comsol.com.
¹⁹T. T. Tsong, *Surf. Sci.* **85**, 28 (1979).
²⁰M. G. Ancona, *J. Vac. Sci. Technol. B* **14**, 1918 (1996).
²¹N. A. Djuzhev, G. D. Demin, P. Yu. Glagolev, M. A. Makhboroda, and N. N. Patyukov, *Proceedings of the 31th International Vacuum Nanoelectronics Conference*, Kyoto Research Park, 9–13 July 2018 (IEEE, Kyoto, 2018), pp. 116–117.